ELSEVIER

Thin Solid Films 382 (2001) 172–182

thin solid films

www.elsevier.com/locate/tsf

MeV Si^+ irradiation of Ni/Fe multilayers: structural, transport and magnetic properties

T. Veres[a], M. Cai[a], R.W. Cochrane[a,*], M. Rouabhi[a], S. Roorda[a], P. Desjardins[b]

[a] *Département de physique et Groupe de recherche en physique et technologie des couches minces, Université de Montréal, C.P. 6128, Succ. Centre-ville, Montréal, Québec H3C 3J7, Canada*

[b] *Materials Science and Engineering Department, Coordinated Science Laboratory, Materials Research Laboratory, University of Illinois at Urbana–Champaign, 1101 W. Springfield, Urbana, IL 61801, USA*

Received 25 August 1999; received in revised form 3 August 2000; accepted 18 September 2000

Abstract

The modification of the structural, transport and magnetic properties of Fe(28 Å)/Ni(85 Å) multilayers on 1-MeV Si^+ irradiation at low temperature (77 K) has been studied as a function of dose. The as-deposited multilayers exhibit a strong Ni(111)/Fe(110) texture with sharp interfaces. Upon irradiation, progressive intermixing at the interfaces is clearly observed in the low-angle X-ray reflectivity and quantified by fitting the data with a standard optical model incorporating interface roughness, intermixing and individual layer thickness fluctuations. Simultaneously, the average grain size gradually increases from ~ 170 to ~ 250 Å with increasing ion dose up to 3×10^{16} ions cm^{-2}. These changes lead to an increase in the anisotropic magnetoresistance from $\sim 1.4\%$ in the as-deposited sample to $\sim 1.8\%$ after irradiation with a dose of 10^{16} ions cm^{-2}, and to the establishment of an in-plane easy axis for the magnetization. The effect of ion bombardment on the transport properties are explained using a model based on the Boltzmann equation incorporating the intermixing characteristics determined from the quantitative X-ray analyses.

Keywords: Interfaces; Magnetic properties and measurements; Resistivity; Structural properties

1. Introduction

Magnetic thin films and multilayers are currently of interest for use as low-field magnetic sensors due to their unique magnetic and transport properties. Considerable effort is being deployed in order to understand and to optimize the giant magnetoresistance (GMR) and the anisotropic magnetoresistance (AMR) of multilayer systems combining ferromagnetic (F) layers with non-magnetic (N) or other ferromagnetic (F) ones. A strong driving force behind these studies can be found in the technological potential of these materials, arising from their large sensitivities to magnetic fields.

Recently, a large AMR field sensitivity ($\sim 0.18\%$ Oe^{-1}) at room temperature was reported for Ni(42 Å)/Co(48 Å) multilayers grown on sapphire substrates by molecular beam epitaxy [1]. Theoretical work by Smit [2], and Potter [3] has shown that the spin–orbit interaction of the conduction electrons in a ferromagnetic metal gives rise to an anisotropic scattering potential, leading to a dependence of the resistivity on the angle between the current and the sample magnetization. Experimental investigations by McGuire and Potter [4] and Jaoul et al. [5] demonstrated that ferromagnetic alloys based on Co, Ni, and Fe exhibit a large AMR, with possible applications for magnetic recording. They found that the most suitable candidates for

* Corresponding author.
E-mail address: cochrane@phys.umontreal.ca (R.W. Cochrane).

0040-6090/01/$ - see front matter
PII: S0040-6090(00)01700-4

sensor applications are *bulk* NiFe alloys with compositions in the permalloy region near $Ni_{80}Fe_{20}$ (AMR ≈ 4% at room temperature); these alloys have the additional benefits of low coercivity and very small magnetostriction. In thin film samples, however, the value of the AMR is limited to approximately 2%, due to the strong scattering at the outer surface [6].

The advantage of multilayered structures is the flexibility to tailor the transport and magnetic properties in order to obtain high saturation magnetization, low coercivity and small magnetostriction. The magnetic properties of the multilayers, in particular the magnetostriction and the AMR, depend strongly on the crystalline quality and the roughness at the interfaces between layers. For example, Gallego et al. [7] found strong superlattice effects in Ni/Co multilayers, with at least eight periods in which resistivity and AMR oscillations are observed as a function of layer thickness. Theoretical and experimental results [8] also indicate that a large interfacial anisotropy can occur in [111] f.c.c. polycrystalline Co/Ni multilayers composed of thin (4–12 Å) layers; this anisotropy can lead to perpendicular magnetization and a larger saturation moment than obtained in Co/X (X = Pd, Pt, Au) F/N multilayers.

Among F/F systems, Ni/Fe bilayers and multilayers are particularly attractive due to the soft magnetic behavior (low coercivity and magnetostriction, high remanence and low saturation fields) that can be achieved by controlling the atomic and magnetic structure in the interfacial region during growth, or through subsequent interdiffusion process steps. The effects of interdiffusion and layer thickness on the magnetostriction in Ni/Fe multilayers have been previously reported [9]. It was found that a very small magnetostriction can be achieved via the interplay of the magnetostrictions of the Ni, Fe, and Ni–Fe intermixed layers. Ehrlich et al. [10] have shown that multilayered polycrystalline Ni/Fe samples with individual layer thicknesses large enough to retain the bulk crystal structure (> 30 Å) possess transport properties similar to those of the bulk ferromagnetic films. Fe layers thinner than ~30 Å, however, could be grown in an f.c.c. phase stabilized by the Ni underlayers, causing such samples to exhibit a more complicated magnetic structure due to changes in the magnetic anisotropy in the interfacial regions.

Ion beam irradiation (IBI) can modify the interfacial regions of multilayer structures in a controlled fashion as a result of ion–solid interactions. While electronic interactions transfer energy to bound and free electrons, nuclear collisions can lead to permanent atomic displacements from the original lattice positions. Thus, significant ion-induced interfacial mixing can occur in multilayers. The fractional energy losses via electronic and nuclear processes are determined by the masses of the incident and target atoms [11]. In addition to these ballistic parameters, thermodynamic properties, such as heat of mixing and cohesive energy, as well as external variables, such as temperature, can also influence the mixing efficiency [12].

In this paper, we concentrate on the evolution of the structural, magnetic, and transport properties of a Ni/Fe multilayer with average atomic composition in the permalloy region induced by bombardment with 1-MeV Si^+ ions. Progressive intermixing at the interfaces as the ion dose is increased from 10^{13} to 3×10^{16} ions cm^{-2} is quantified using specular X-ray reflectivity (XRR) and diffraction (XRD) analyses. The evolution of the transport properties, in particular the resistivity and the AMR, is modeled using a charge transport model based on the Boltzmann equation, incorporating the exact multilayer characteristics determined from the structural analysis.

2. Experimental details

Multilayer samples with the configuration [Fe(28 Å)/Ni(85 Å)]$_{11}$ were deposited on thermally oxidized Si(100) wafers by RF triode sputtering [13]. In order to simplify the notation, these multilayers are hereafter referred to as Fe_{28}/Ni_{85}. Prior to sputtering, the system was cryopumped to a base pressure of 10^{-7} torr; sputtering was carried out at an RF power of 200 W and an Ar pressure of 3 mtorr onto a substrate maintained at 40 ± 3°C. These conditions resulted in deposition rates of 0.8 and 1.2 Å s^{-1} for Fe and Ni, respectively. A rectangular sample geometry, 4×15 mm^2 with thin side arms on each side distanced 8 mm apart, was defined by deposition through a contact mask.

XRR measurements were performed in a Philips system with a four-crystal Bartels Ge monochromator in the 220 configuration and Cu-$K_{\alpha 1}$ radiation (λ = 1.540597 Å); XRD analyses were carried out with an automated Nicolet-Stöe L11 powder diffractometer using Cu-K_α radiation. The magnetization was measured at room temperature using a vibrating sample magnetometer operating at 85 Hz with a resolution of better than 10^{-5} e.m.u. Transport properties (resistivity and anisotropic magnetoresistance) were determined using a standard four-point method on a high-resolution AC-bridge. For both magnetic and magnetotransport measurements, the external field was applied in the sample plane. In the following, by *longitudinal* and *transverse* we denote either magnetoresistance or magnetization measurements with the magnetic field oriented along the length of the sample and perpendicular to this direction, respectively.

Normal incidence IBI was performed at a pressure near 10^{-7} torr with 1-MeV Si^+ ions rastered over an area of 2.5×2.5 cm^2 using the Université de Montréal Tandetron accelerator. To avoid sample heating during irradiation, the beam current was kept below 50 nA

cm^{-2} and the samples were placed in thermal contact with a copper block maintained at 77 K. The dose Φ was systematically increased from an initial value of 10^{13} to a final value of 3×10^{16} cm^{-2}. At each stage, the irradiation was performed simultaneously on the Fe_{28}/Ni_{85} multilayer and on reference 1000-Å Fe and 1500-Å Ni films, also deposited on oxidized Si(100) substrates. The ion energy of 1 MeV was selected such that the projected ion range was much larger than the total film thickness (1200 Å); consequently, a uniform mixing profile throughout the multilayer is expected. TRIM simulations [14] give a projected ion range of 1.5 μm and indicate that only a very small fraction ($< 0.1\%$) of the implanted ions remain within the magnetic films, the rest being transmitted or backscattered.

3. Results and discussion

3.1. High-angle X-ray diffraction

Fig. 1 presents selected XRD curves for Fe_{28}/Ni_{85} as a function of the ion dose. The curve for the as-deposited multilayer exhibits a strong peak located at $2\theta = 44.5°$, very close to the expected positions for the (111) f.c.c. Ni ($2\theta = 44.60°$) and (110) b.c.c. Fe ($2\theta = 44.66°$) reflections, but characterized by a slightly larger interplane separation perpendicular to the film surface than the equilibrium structures of either element. No other f.c.c. or b.c.c. peaks are visible in the interval up to 65°; in particular the f.c.c. (200) peak at approximately 52° is absent. Combining these results with earlier studies [15,16] leads to the conclusion that the film is strongly Ni(111)/Fe(110) textured in the growth direction. Superlattice diffraction peaks are visible around the principal Ni/Fe peak, indicating that the crystalline coherence length in the growth direction is larger than the superlattice period. A number of other peaks that arise from the interaction of the Ni and Fe with the substrate or the atmosphere are also observed.

Several effects of ion bombardment should be noted from Fig. 1. The first is the shift of the (111/110) peak position toward lower angles upon irradiation, indicating that the average lattice parameter in the growth direction, $a_\perp$, increases with dose. Assuming an f.c.c. structure for the crystals, the lattice parameter of the as-deposited sample equals 3.525 Å, somewhat larger than that of bulk f.c.c. Ni (3.517 Å), a fact which might indicate the presence of a small in-plane compressive strain. No significant changes in the lattice parameter are apparent for doses up to 5×10^{13} ions cm^{-2}. At higher doses, $a_\perp$ increases monotonically to reach a value of 3.565 Å at the maximum dose of 3×10^{16} ions cm^{-2} as a result of progressive intermixing of the two elements driven by a negative enthalpy of mixing. This variation is consistent with the measured lattice

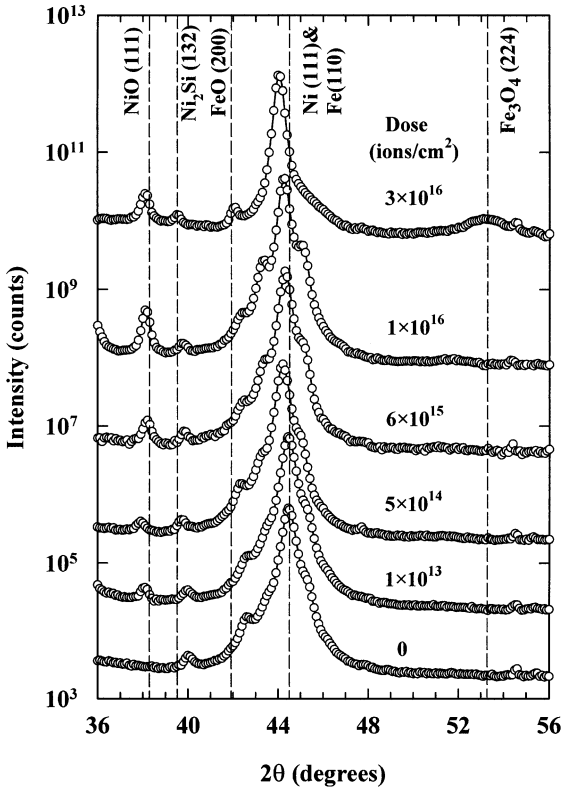

Fig. 1. High-angle θ-2θ XRD curves for the Fe_{28}/Ni_{85} multilayer as a function of ion dose Φ. The acquisition time per step was 80 s. Successive curves have been shifted vertically for clarity.

parameters of f.c.c. Ni–Fe alloys, which rise linearly from 3.517 Å for Ni to a maximum of 3.589 Å at 39 at.% Ni [17–19] before decreasing again in the Invar region of the Fe-rich f.c.c. alloys.

The multilayer period Λ_h has been calculated from the spacing between superlattice peaks using the relationship:

$$\frac{2\sin\theta}{\lambda_{Cu}} = \frac{1}{d} \pm \frac{n}{\Lambda_h} \quad (1)$$

where n is the order of the satellite around the main Bragg peak ($n = 0$) and d is the interatomic layer spacing between (111) planes. Λ_h values calculated from the XRD data are summarized in Table 1, along with those determined from XRR measurements (see Section 3.2).

The second effect attributed to IBI is grain coarsening, which results in a decrease of the linewidth of the Bragg peaks as the dose increases (Fig. 1). Fig. 2 presents the evolution of the grain size D in the growth direction, obtained using the Scherrer formula [20]. D remains approximately constant at ~ 170 Å, slightly larger than the multilayer period, for Φ up to 5×10^{14} ions cm^{-2} and, thereafter, increases continuously by

Table 1
Structural parameters as a function of ion dose[a]

Dose Φ (10^{14} ions cm^{-2})	Λ_h (±2) (Å)	Λ_l (Å)	W (Å)	σ_i (Å)	t_{oxide} (Å)	σ_s (Å)
0	112	111.6 ± 0.4	6.6 ± 0.2	3.7 ± 0.2	28.1 ± 0.3	3.6 ± 0.2
0.1	112	111.8 ± 0.5	10.3 ± 0.2	3.7 ± 0.1	27.8 ± 0.4	3.5 ± 0.2
0.5	—	112.3 ± 0.6	12.3 ± 0.3	4.1 ± 0.2	28.7 ± 0.3	5.0 ± 0.2
1.0	113	112.1 ± 0.6	16.7 ± 0.2	6.9 ± 0.2	28.8 ± 0.3	4.7 ± 0.2
5.0	113	112.4 ± 0.8	20.9 ± 0.3	6.3 ± 0.2	38.5 ± 0.4	4.9 ± 0.4
30	—	112.7 ± 0.6	26.1 ± 0.3	5.8 ± 0.2	42.6 ± 0.6	7.6 ± 0.2
60	113	112.9 ± 0.5	32.9 ± 0.3	6.1 ± 0.4	45.3 ± 0.4	9.0 ± 0.1
100	112	111.3 ± 1.3	38.8 ± 0.9	11.0 ± 0.7	51.4 ± 0.5	11.8 ± 0.2
300	—	110.9 ± 2.4	55.2 ± 2.2	19.9 ± 2.5	72.5 ± 0.4	9.3 ± 0.1

[a]The superlattice period Λ_h determined from the XRD superlattice peaks and the superlattice period Λ_l, obtained from the XRR simulations as well as the intermixing width W, the interface roughness σ_i, the surface oxide layer thickness t_{oxide} and the substrate roughness σ_s.

almost 50% to reach ~250 Å at maximum dose. Such grain growth has been previously reported in thin Ni films bombarded with different ions (Ag^+, Ar^+, Kr^+, and Xe^+) at energies ranging from 240 to 560 keV [21–23]. We have also observed such coarsening in cross-sectional and plane-view transmission electron microscopy (TEM) images on a series of Ni(500 Å)/Fe(500 Å) bilayers irradiated under similar conditions [24]. As suggested by Liu and his colleagues [25,26], IBI-induced grain growth can be understood in a manner similar to grain boundary migration in a deformed metal during recrystallization. In their picture, relatively undamaged grains act as nucleation sites for growth into the damaged region. Since the probability of damaging an entire grain is high for small grains, the larger grains consume the smaller, and the average grain size increases. This model, however, relies only on collisional properties to explain grain growth and requires recrystallization, an unlikely scenario for metal irradiation at 77 K. To circumvent these difficulties, Liu et al. [25,26], followed by Alexander et al. [27], proposed that grain growth during heavy-ion irradiation of fine-grained thin films could be interpreted as boundary migration during thermal spikes. The kinetic energy of the recoils during a cascade is thermalized in the lattice, resulting in the formation of thermal spikes in localized areas. A spike that occurs near a grain boundary leads to atomic jumps, and could result in a net boundary motion.

Additional reflections appear as the dose increases, in particular, a small intensity peak near $2\theta = 38°$ becomes visible after the initial dose of 10^{13} ions cm^{-2} and grows systematically with further irradiation. This peak is close to the expected position for f.c.c. NiO(111). Since its presence is clearly established well before Ni completely mixes into the top Fe layer ($> 6 \times 10^{15}$ ions cm^{-2}), the initial formation of this NiO layer must occur at the substrate/Ni interface. The minor peak at approximately 40° in all the curves can be associated with Ni_2Si(132) at the same interface. Since the Ni–SiO_2 system has been shown to be stable during conventional thermal anneals, our results indicate that 1-MeV ion-beam irradiation leads to significantly different reaction pathways that are probably the result of atom motion following collisions. Finally, the oxidation of the Fe cap-layer after irradiation with 3×10^{16} ions cm^{-2} is evidenced by the presence of small FeO(200) ($2\theta = 42.1°$) and Fe_3O_4(224) ($2\theta = 53.2°$) peaks.

3.2. Specular low-angle X-ray reflectivity

Low-angle XRR measurements of the Fe_{28}/Ni_{85} multilayer are shown in Fig. 3 at various stages of ion bombardment. Beyond the critical wave vector (Q) for total reflection, the intensity falls off abruptly ($\sim Q^{-4}$) with a series of finite-thickness interference fringes and superlattice peaks superimposed on the falling background. The amplitudes and persistence of both sets of oscillations are functions of the electron-density contrast and the sharpness of the individual layers.

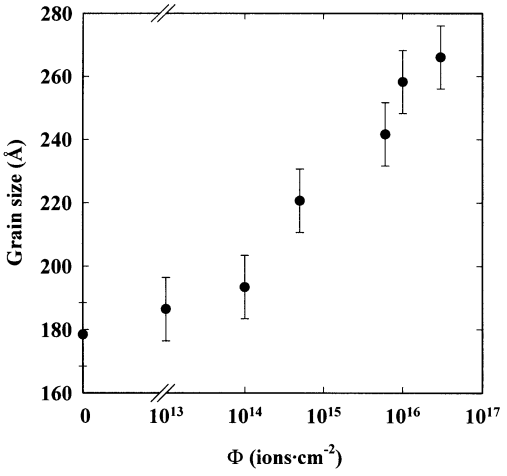

Fig. 2. Average grain size in the growth direction as a function of the ion dose Φ as calculated from the high-angle XRD curves using the Scherrer formula.

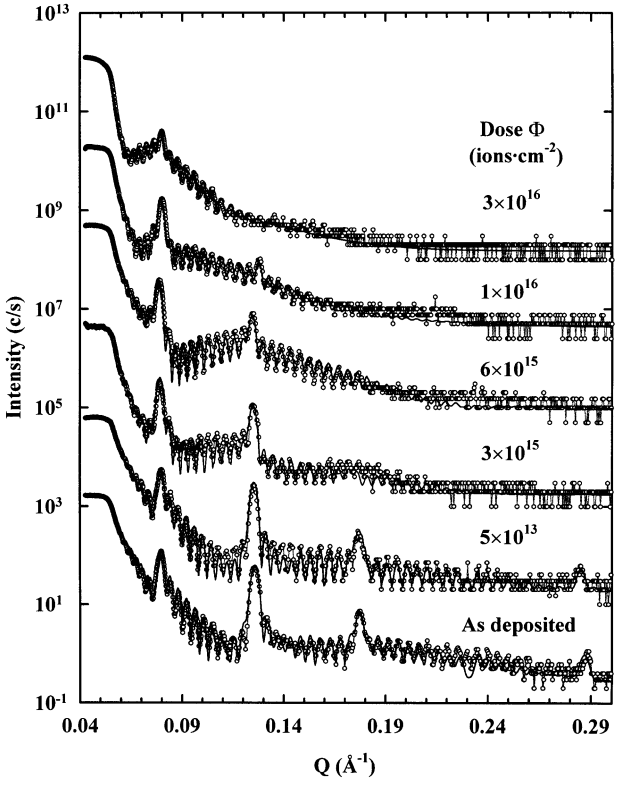

Fig. 3. XRR curves for the Fe_{28}/Ni_{85} multilayer as function of the ion dose Φ. The open circles are experimental data, while the solid lines are fitted curves. Successive curves have been shifted vertically by one decade for clarity.

For the as-deposited multilayer, superlattice peaks are observed up to the fifth order, confirming that the Ni/Fe interfaces are flat and parallel to the substrate surface and that the bilayer thickness is reasonably uniform throughout the multilayer. The absence of the fourth-order peak is expected for a 3:1 thickness ratio between the Ni and Fe sublayers. A low-amplitude long-wavelength oscillation is superimposed on the overall profile of the curves, and can be attributed to a thin layer of surface oxide formed during exposure of the sample to the atmosphere after deposition. The intensities of the superlattice peaks in Fig. 3 are progressively reduced as the ion dose increases. However, even at the maximum dose of 3×10^{16} ions cm^{-2}, a weak first-order peak can still be observed, revealing that a compositionally modulated structure persists to some extent. In addition, the total-thickness peaks are also visible, from which it can be concluded that an abrupt interface between the multilayer and the SiO_2 substrate is preserved, even though the Fe and Ni layers have been substantially mixed.

The effects of IBI on the multilayer structure and interfaces have been quantified by fitting the XRR data using a standard optical model [28] based on the recursive theory of Parratt [29]. In this model, the multilayer is considered to consist of a stack of individual layers, each having a constant electron density, and the reflectivity for the whole heterostructure is calculated using a matrix method [30]. In order to include interfacial mixing, each interface is treated as a sequence of slices (~1 monolayer thick) with a linear variation of the electron density and the absorption coefficient from one side of the interface to the other. Roughness values at the top surface and at each interface are modeled as Gaussian distributions of the interface position and are directly incorporated into the calculation by multiplying a Debye–Waller factor $\exp(-\sigma_i^2 Q^2)$ into the appropriate multilayer reflectivity. σ_i measures the rms roughness. Model calculations were fitted to the data using the non-linear least-squares procedure described in [30].

Although many parameters are involved in the fitting procedure, convergence to a unique set is obtained in each case. Since the positions and intensities of the superlattice peaks are very sensitive to the parameters characterizing the interface, namely the individual layer thickness (t_{Ni} and t_{Fe}), the width of the linearly graded interfacial region (W) and the Gaussian interface roughness (σ_i), the fitting procedure provides well-defined values for them. Parameters, such as the oxide thickness (t_{oxide}) and its roughness (σ_{ov}), as well as the substrate roughness (σ_s), influence the overall profile of the reflectivity curves, but have little effect on the intensities of superlattice peaks. Increasing σ_{ov} and σ_s leads to a faster decrease in the reflected intensity and to a reduction of the amplitude of the total thickness fringes as the scattering wave vector increases. In addition, the presence of an oxide overlayer introduces extra oscillatory features, for which the wavelength is inversely proportional to the layer thickness. As shown in Fig. 3, such an oscillation is evident near the second-order superlattice peak after irradiation at 3×10^{15} ions cm^{-2}. At this dose, t_{oxide} is calculated as 45 ± 3 Å; it evolves towards 73 Å at the maximum dose.

The calculated curves are shown as solid lines in Fig. 3, where it is seen that the agreement between experimental and calculated curves with respect to both the position and the intensity of the peaks is excellent for all ion doses. The principal fitting parameters are presented in Table 1 for the as-deposited and irradiated samples. Upon irradiation, the intermixing width W increases from 7 Å for the as-deposited sample to 26 Å at a dose of 3×10^{15} ions cm^{-2}, at which point the entire Fe layer is mixed and the multilayer consists of only Ni and NiFe alloy regions. At maximum dose, the intermixing width reaches half of the modulation wavelength (~55 Å) and the pure Ni layer is completely consumed. The sample has become a compositionally modulated alloy structure.

Fig. 4 shows that the square of the irradiation-induced intermixing width $W_{ion}^2 = W^2 - W_0^2$, where W_0, the zero-dose width, varies linearly with ion dose, as

predicted by the cascade model of ion beam mixing [31]. A value of approximately 300 Å^4 is obtained for the ion-beam mixing efficiency $d(W_{ion}^2)/d\Phi$, and can be compared with that calculated from the theory of collisional mixing developed by Sigmund and Gras-Marti for ballistic ion beam mixing [32]:

$$\frac{d(W_{ion}^2)}{d\Phi} = \frac{2}{3}\Gamma_0 \xi \frac{F_D R_c^2}{\delta E_d} \quad (2)$$

where $\Gamma_0 = 0.608$ is a dimensionless parameter, ξ is a mass-sensitive kinematic factor given by $[4M_1M_2/(M_1+M_2)^2]^{1/2}$ where M_1 and M_2 are the masses of the atoms involved in collisions, R_c^2 is the mean squared range of a displaced atom, taken here to be 100 Å^2 [33]. E_d is the threshold displacement energy, δ is the average atomic density and F_D is the energy deposited per unit length due to nuclear collisions. Typical values for the pertinent parameters are $E_d = 20$ eV (the average for Ni and Fe [34]), $F_D = 25$ eV Å^{-1} (obtained from TRIM simulation), and a kinetic factor averaged for the composition of the multilayer $\xi = [x\xi_{Ni} + (1-x)\xi_{Fe}]$, x being the Ni fraction.

Using these values, Eq. (2) gives a mixing efficiency of 540 Å^4. The difference between theoretical and experimental values of the mixing efficiency is attributed to finite thickness effects related to the multilayer structure, which are not accounted for in the simple model. For example, intermixing initially occurs between Ni and Fe layers and subsequently between Ni and a Ni–Fe mixture.

3.3. Magnetic properties

The magnetization of the as-deposited Fe_{28}/Ni_{85} multilayer is isotropic within the plane of the sample, as indicated by the very similar magnetization-field curves measured in the longitudinal and transverse configurations (Fig. 5a). The magnetic moment saturates in relatively low fields ($\sim$ 15 Oe), with a coercivity in both directions of approximately 8 Oe and a remanent magnetization M_r of approximately 80% of the saturation value M_s. IBI has several effects on the magnetic behavior of this sample, the most noticeable being the development of an easy axis in the transverse direction. Fig. 5b shows the magnetization curves after an ion dose of 6×10^{15} ions cm^{-2}. At this point, the longitudinal magnetization requires a much higher field for saturation ($\sim$ 30 Oe), while its remanence has dropped to approximately 45% of M_s. In the transverse direction, the saturation field has fallen to $\sim$ 10 Oe and the remanence has grown to $\sim$ 95% of M_s. Since the presence of NiO, which is antiferromagnetic, has been detected in the sample after irradiation, coupling between antiferromagnetic NiO and ferromagnetic Ni–Fe is a possible mechanism for the establishment of the easy axis.

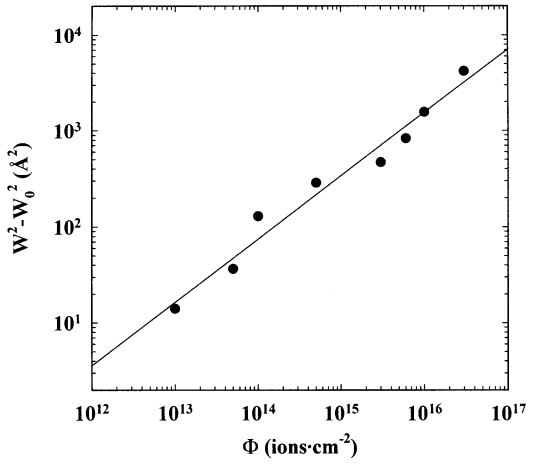

Fig. 4. The square of the irradiation-induced intermixing width $W^2 - W_0^2$ obtained from fitting of the XRR curves, as a function of the ion dose Φ.

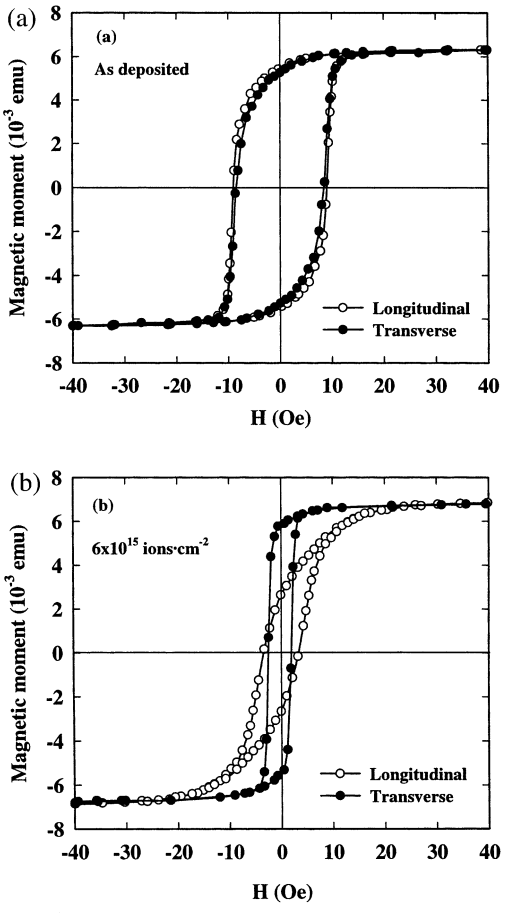

Fig. 5. Magnetization curves for the Fe_{28}/Ni_{85} multilayer, measured at 300 K, in longitudinal (○) and transverse (●) geometries for (a) the as-deposited sample and (b) after irradiation with $\Phi = 6 \times 10^{15}$ ions cm^{-2}.

In parallel with the changes outlined above, the coercivity, H_c, decreases from ~ 8.2 Oe in the as-deposited multilayer to ~ 2 Oe after irradiation at 6×10^{15} ions cm^{-2} (Fig. 5). The variation in H_c with ion dose is detailed in Fig. 6, along with the behavior of pure Ni and Fe films irradiated simultaneously. This figure clearly demonstrates that the normalized coercivity $H_c/H_c(0)$, with $H_c(0)$ being the coercivity at zero-dose, decreases more rapidly for the multilayer than the pure films. A decrease in H_c with increasing grain size, approximately following a $H_c \sim 1/D$ dependence, was observed in polycrystalline NiFe and CoFe alloys [35] and was explained by domain-wall pinning at grain boundaries that become progressively less efficient as the volume fraction of grain boundaries decreases. However, this effect should be similar for multilayers and the pure Ni and Fe films. The more pronounced decrease of $H_c/H_c(0)$ in the multilayered sample can be attributed to a progressive intermixing at the interfaces, which leads to the formation of an NiFe alloy magnetically softer than the individual elements.

3.4. Transport properties

3.4.1. Experimental results

The AMR of Fe_{28}/Ni_{85}, as-deposited and after irradiation at 10^{16} ions cm^{-2}, are illustrated in Fig. 7a. These curves are obtained by rotating the magnetic field at saturation between the longitudinal and transverse orientations. Since the magnetization lies in the film plane, only one direction of the magnetization perpendicular to the current is allowed, so that the average resistivity is defined as $\rho_0 = (\rho_{\parallel} + \rho_{\perp})/2$. As for most ferromagnetic films, including NiFe alloys [4], the total anisotropic magnetoresistivity $\Delta\rho = \rho_{\parallel} - \rho_{\perp}$, calculated at saturation, is positive; its amplitude does not depend on the magnetic domain structure or the mechanisms involved in the magnetization process [36]. However, usefulness as a magnetic sensor is determined by the variation in $\Delta\rho_{\parallel}$ and $\Delta\rho_{\perp}$ with fields below saturation, and hence on the mechanisms (wall displacements, coherent rotations) involved in the magnetization process. Large amplitudes for $\Delta\rho_{\parallel}$ and $\Delta\rho_{\perp}$ can be expected in samples in which the magnetization process is dominated by in-plane rotations of the magnetic moments.

For the as-deposited sample presented in Fig. 7a, the amplitudes of both the parallel ($\Delta\rho_{\parallel} \sim 0.23$ $\mu\Omega$ cm) and perpendicular magnetoresistivities ($\Delta\rho_{\perp} \sim 0.27$ $\mu\Omega$ cm) are comparable to the total anisotropic magnetoresistivity $\Delta\rho$ (~ 0.32 $\mu\Omega$ cm), demonstrating that the magnetization process for both field orientations is

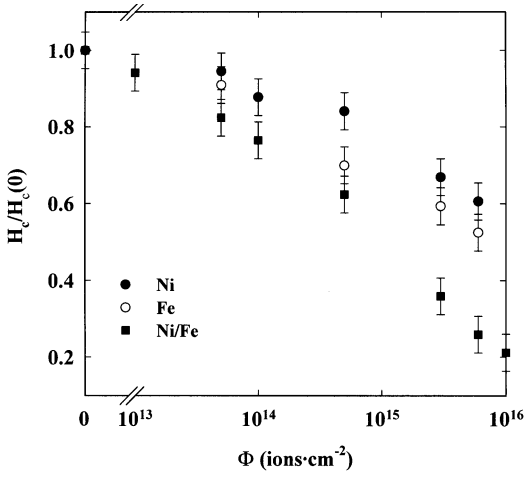

Fig. 6. Longitudinal coercivity for the Fe_{28}/Ni_{85} multilayer and for 1000-Å Fe and 1500-Å Ni single-layer films as a function of the ion dose Φ.

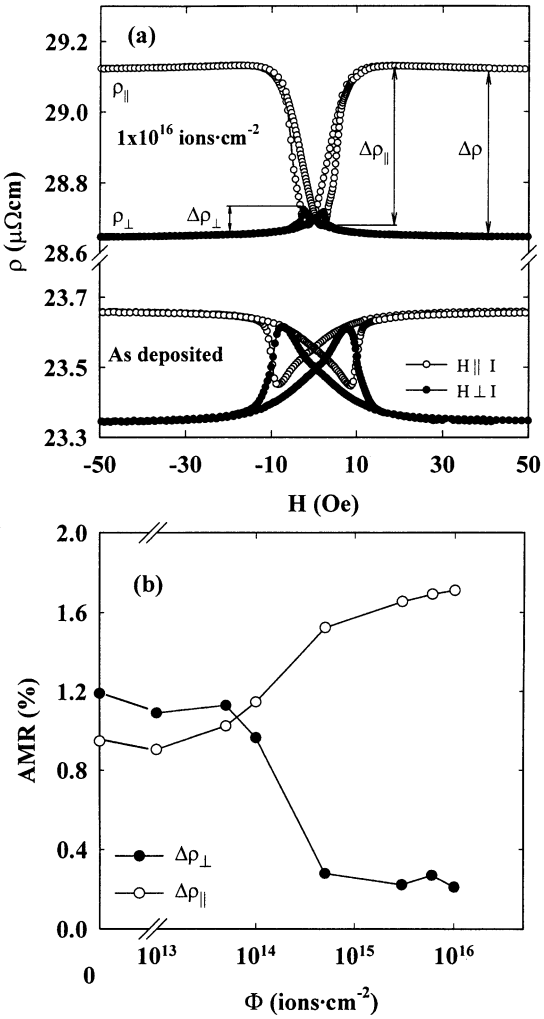

Fig. 7. (a) Resistivity at 300 K for the Fe_{28}/Ni_{85} multilayer as a function of the intensity of the magnetic field H applied parallel ($\rho_{\parallel}$) and perpendicular ($\rho_{\perp}$) to the current, before irradiation and after irradiation with $\Phi = 1 \times 10^{16}$ ions cm^{-2}; and (b) the variation of the parallel $\Delta\rho_{\parallel}/\rho_0$ and perpendicular $\Delta\rho_{\perp}/\rho_0$ AMR ratios as function of the ion dose Φ.

dominated by in-plane rotations of the magnetic moments rather than domain-wall displacements. The $\rho_{\parallel}(H)$ and $\rho_{\perp}(H)$ values saturate in fields comparable to those of the magnetization, and peaks appear in both curves at fields identical with the corresponding coercivity (~ 8 Oe). After irradiation, $\Delta\rho_{\parallel}$ is much larger than $\Delta\rho_{\perp}$, confirming the presence of an easy axis in the transverse direction. During the field sweep in the longitudinal direction, the magnetization actually rotates 90° into the transverse direction at small fields. However, for the field oriented in the transverse direction, the magnetization process is controlled by domain-wall displacements with little moment rotation, and thus little change in the resistivity. Fig. 7b shows the evolution of this phenomenon with ion dose, and reveals a threshold dose of the order of 10^{14} and a saturation near 10^{15} ions cm^{-2}. The field sensitivity, defined as $(\Delta\rho_{\parallel}/\rho_0)/(\Delta H)$, with ΔH being the full width at half-maximum for the MR peak, at maximum dose is 0.18% Oe^{-1}, comparable with that reported for Ni/Co multilayers by Gallego et al. [1].

Fig. 8 shows ρ and the AMR as functions of Φ for the multilayer as well as for the single-layer Ni and Fe films. While the resistivities of neither Ni nor Fe change with ion dose, that of the multilayer increases progressively from 23.3 to 28.6 $\mu\Omega$ cm. Consequently, the increase in multilayer resistivity can be associated with mixing at the Ni/Fe interfaces [4] rather than to bulk defects produced by ion irradiation. As noted in Section 3.1, the grain size increases from 170 to 250 Å upon irradiation. On the one hand, this increase leads to a decrease in the film resistivity through a diminution of the number of gain-boundary scattering events. On the other, it is offset by the significant increase in scattering from impurity atoms (Ni in Fe, or Fe in Ni) in the interface region, since the grain size ($D \sim 150$ Å) is much larger than electron mean free-paths in both the Ni ($\lambda_{Ni} \sim 35$ Å) and the Fe ($\lambda_{Fe} \sim 15$ Å) layers.

Finally, the AMR for the as-deposited Fe and Ni films are ~ 0.15 and $\sim 1.5\%$, respectively, in agreement with previously reported values [4]. While these values remain almost unchanged upon irradiation, the AMR of the multilayer rises to $\sim 1.8\%$ at a dose of 10^{16} ions cm^{-2}. This behavior underscores the formation of NiFe alloys, which are known to have an AMR larger than that of the two constituents. Indeed, the AMR attains its maximum value for this alloy system in the permalloy region [4,37].

3.4.2. Model calculations

In order to obtain quantitative information about electron scattering in the interfacial regions created by the IBI, we adopt a semi-classical model based on the Boltzmann transport equation as proposed by Carcia and Suna [38]. The multilayer is described as a repeated structure of two ferromagnetic layers with thick-

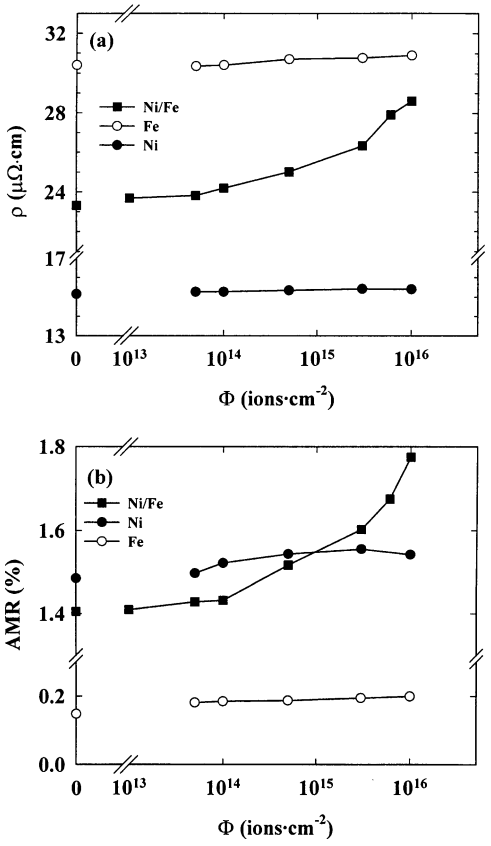

Fig. 8. (a) Resistivity and (b) AMR ratio measured at 300 K as a function of ion dose Φ for the Fe_{28}/Ni_{85} multilayer, as well as for 1000-Å Fe and 1500-Å Ni single-layer films.

ness t_1 and t_2. The electric field E is applied in the film plane along the longitudinal (x) direction and the current is determined within each layer by the spin-dependent electron distribution function $f_i\sigma(\overset{\rho}{v},z)(i = 1,2)$, which depends only on the co-ordinate perpendicular to the film (z) and the velocity v:

$$f_{i\sigma}\left(\vec{v},z\right) = f^0_{i\sigma}\left(\vec{v},z\right) + g_{i\sigma}\left(\vec{v},z\right) \tag{3}$$

Here $f^0_{i\sigma}(\overset{\rho}{v},z)$ is the equilibrium (zero-field) distribution function and $g_{i\sigma}(\overset{\mu}{v},z)$, the deviation from equilibrium due to the applied field. Following the general method [38–40], we divide g into two parts: $g^+_{i\sigma}(\overset{\rho}{v},z)$ for electrons with $v_z > 0$, and $g^-_{i\sigma}(\overset{\rho}{v},z)$ for those with $v_z < 0$. The general solution of the Boltzmann equation in the relaxation time approximation takes the form:

$$g^{\pm}_{i\sigma} = \frac{|e|\,E}{m}\cdot\frac{\partial f^o_{i\sigma}\left(\vec{v}\right)}{\partial z} \times\left\{1 + F^{\pm}_{i\sigma}\left(\vec{v}\right)\exp\left[\mp\frac{z}{\tau_i|v_z|}\right]\right\} \tag{4}$$

in which $\tau_{i\sigma}$, is the relaxation time in layer i for spin σ, e and m are the electron charge and mass, respectively. The functional form of $F_{i\sigma}^{\pm}$ is obtained by requiring the electron distribution function to satisfy the boundary conditions, which are written, for $v_z > 0$, as:

$$g_{1\sigma}^{+}(0^{+}) = Tg_{2\sigma}^{+}(0^{-}), \quad \text{at } z = 0 \tag{5}$$

$$g_{2\sigma}^{+}(t_1^{+}) = Tg_{1\sigma}^{+}(t_1^{-}), \text{ at } z = t_1 \tag{6}$$

where T is the transmission coefficient which depends on the incident angle (φ) of the electron at the interface according to:

$$T = T_0 \cos(\varphi) \tag{7}$$

In order to calculate the AMR, we assume a cosine squared dependence of the mean free path ($\lambda_{i\sigma}$ i = Ni or Fe, σ, spin) on the angle θ between the electron velocity v and the magnetization M_s [41] according to:

$$\lambda_{\sigma i} = \lambda_{i\sigma}^{0}\left[1 + \alpha_{i\sigma} \cdot \cos^2(\theta)\right] \tag{8}$$

with anisotropic scattering factors $\alpha_{i\sigma}$. The current density (J) along the electric field in each layer is found by integrating the solution of the Boltzmann equation over the velocity space to yield:

$$J_{x,i\sigma}(z) = -|e|\left[\frac{m}{h}\right]^3 \int v_x g_{i\sigma}\left(\vec{v}, z\right) d^3\vec{v} \tag{9}$$

in which h is Planck's constant. The effective conductivity is found by averaging over the whole film according to:

$$\sigma = \frac{1}{E(t_1 + t_2)} \sum_{i=1}^{2} \sum_{\sigma = \uparrow \downarrow} \int J_{x,i\sigma}(z) \mathrm{d}z \tag{10}$$

For simplicity in the numerical calculations, the spin-up and spin-down electrons are treated equivalently, using average values of the mean free path and the asymmetry scattering factor for the two spin channels of each magnetic layer. By fitting the thickness dependence for ρ and AMR using the model described above, we have obtained the mean free paths and the anisotropic scattering factors for Ni and Fe in the as-deposited samples. Since the bulk magnetoresistance of Ni is 10-fold larger than that of Fe, the anisotropic electron scattering is assumed to arise solely from the Ni layers and α_{Fe}, is set to zero in the subsequent analysis.

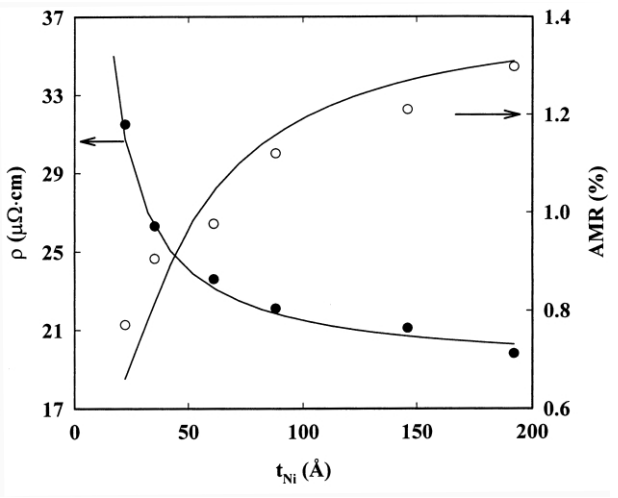

Fig. 9. Anisotropic magnetoresistance ratio ($\Delta\rho_{\perp}/\rho_0$) and resistivity ($\rho$) as a function of the Ni layer thickness for a series of Fe(x Å)/Ni($3x$ Å) multilayers deposited on oxidized Si(100). The solid lines have been calculated using the semi-classical model with the parameters described in the text.

In Fig. 9 are presented the resistivity ρ and AMR for a series of non-irradiated multilayers with a fixed 3:1 ratio between the Ni and Fe layer thickness; the total thickness was fixed by varying the number of periods of the multilayer. The fitted results presented as solid lines in the figure were calculated with $\lambda_{Ni} = (37 \pm 2)$ Å, $\lambda_{Fe} = (15 \pm 2)$ Å, $T_0 = 0.8 \pm 0.1$ and $\alpha_{Ni} = 0.040 \pm 0.005$ [15,16]. These values of the mean free paths are close to values found from fitting the thickness dependence of the resistivities of the pure film. Only the first three parameters are needed to determine the thickness dependence of the resistivity of the multilayers, the fit depending very sensitively on T_0. Once these parameters are determined, the AMR is fitted with α_{Ni} as the only free parameter. Using these parameters,

Table 2
Anisotropic scattering parameter (α_{NiFe}) and the electron mean-free path λ_{NiFe} for the intermixed region[a]

Dose Φ (10^{14} ions cm^{-2})	λ_{Ni} ($\pm$2 Å)	α_{Ni} ($\pm$0.002)	λ_{NiFe} ($\pm$2 Å)	α_{NiFe} ($\pm$0.002)
0	38	0.040	—	
30			18	0.042
60			19	0.047
100			21	0.052

[a] Obtained from the measured values for the resistivity (ρ) and anisotropic magnetoresistance ratio $\Delta\rho_{\parallel}/\rho_0$ using the semi-classical model. λ_{Ni} and α_{Ni} are the electron mean-free path and the scattering parameter for the Ni layer, respectively.

the resistivity and AMR of the as-deposited Fe_{28}/Ni_{85} multilayer are calculated to be 23.3 $\mu\Omega$ cm and 1.43%, respectively, in excellent agreement with the experimental values of 23.3 $\mu\Omega$ cm and 1.40%.

The threshold for significant changes in ρ and AMR with an ion dose of approximately 10^{14} ions cm^{-2} (see Fig. 8) occurs near the point where the XRR data indicate that the interface width W exceeds the Fe-layer thickness, so that no pure Fe layers remain. In order to fit the transport model to the data for these irradiated multilayers, we replace the Fe-layers with NiFe intermixed layers and make corresponding changes in the model parameters: specifically, λ_{NiFe} replaces λ_{Fe}, and α_{NiFe} is not fixed at zero, as was α_{Fe}. All Ni-related parameters are taken to be independent of dose. λ_{NiFe} and α_{NiFe} are then determined following each irradiation using the data of Fig. 8. The resultant parameters are listed in Table 2, where it is noted that both λ_{NiFe} and α_{NiFe} increase approximately 15–20% with ion dose.

Empirically, McGuire and Potter [4] point out that the AMR increases when Fe is alloyed into Ni to a maximum near the composition $Ni_{0.9}Fe_{0.1}$. In this context, the increase in α_{NiFe} with ion bombardment is consistent with the assumption of alloy formation, which is the basis of the present analysis. However, they have emphasized that the microscopic treatment of AMR involves a complicated combination of elements, including crystal symmetry and band structure, intrinsic parameters, such as the spin–orbit interaction and band splitting energy, as well as extrinsic ones, such as grain size and film thickness. As a result, it is not possible to assign a specific mechanism for the variation of the AMR within the NiFe alloy system.

4. Conclusion

XRR, XRD, magnetization, and magnetotransport measurements all give a consistent picture of the evolution of the structural and magnetic properties of Fe/Ni multilayers irradiated with 1-MeV Si^+ ions. As deposited, the multilayers have a high degree of texture, which is largely preserved under ion bombardment. The principal effect of IBI is to mix the layers progressively from a clearly delineated superlattice up to the point of being almost a uniformly mixed alloy. Not surprisingly, the resulting magnetization and magnetoresistance tend systematically towards those characteristic of the uniform alloy. By constructing a semiclassical model for the electrical transport in multilayers consistent with the structural data, we have been able to parameterize the evolution of the resistivity and the anisotropic magnetoresistance during this transformation.

Acknowledgements

The authors would like to thank R. Morel (CEA Grenoble) for helpful discussions on magnetotransport modeling, M. Sutton (McGill) for valuable assistance with the modeling of the XRR data, L. Cheng (McGill) for help with X-ray diffraction measurements and F. Schiettekatte for his assistance with the ion-beam experiments. This research has received financial support from the Natural Sciences and Engineering Research Council of Canada and the Fonds pour la formation de chercheurs et l'aide à la recherche du Québec.

References

[1] J.M. Gallego, D. Lederman, T.J. Moran, I.K. Schuller, Appl. Phys. Lett. 64 (1994) 2590.
[2] J. Smit, Physica 16 (1951) 612.
[3] R.I. Potter, Phys. Rev. B 10 (1974) 4626.
[4] T.R. McGuire, R.I. Potter, IEEE Trans. Mag. 11 (1975) 1018.
[5] O. Jaoul, I.A. Campbell, J. Fert, J. Magn. Magn. Mater. B5 (1977) 23.
[6] A.F. Mayadas, J.F. Janak, A. Gangulee, J. Appl. Phys. 45 (1974) 2780.
[7] J.M. Gallego, D. Lederman, S. Kim, I.K. Schuller, Phys. Rev. Lett. 74 (1995) 4515.
[8] G.H. Daalderop, P.J. Kelly, F.J.A. den Broeder, Phys. Rev. Lett. 68 (1992) 682.
[9] Y. Nagai, M. Senda, T. Thosima, J. Appl. Phys. 63 (1988) 1136.
[10] A.C. Ehrlich, D.J. Gillespie, T.M. Tritt, C. Kim, A.S. Edelestein, S.B. Qadri, J. Appl. Phys. 70 (1991) 5819.
[11] M. Nastasi, J.W. Mayer, Mater. Sci. Eng. R12 (1994) 1.
[12] W.L. Johnson, Y.-T. Cheng, M. Van Rossum, M.-A. Nicolet, Nucl. Instrum. Methods B 59/60 (1991) 509.
[13] Y. Huai, Ph.D. Thesis, Université de Montréal, 1992, p. 9.
[14] J.F. Ziegler, J.P. Biersack, The Stopping and Range of Ions in Solids, Pergamon Press, New York, 1985.
[15] M. Cai, T. Veres, R. Morel, R.W. Cochrane, J. Appl. Phys. 79 (1996) 6289.
[16] T. Veres, M. Cai, R. Morel, R.W. Cochrane, R. Abdouche, M. Sutton, J. Appl. Phys. 81 (1997) 4758.
[17] E.A. Owen, E.L. Yates, A.H. Sully, Proc. Phys. Soc. (London) 49 (1937) 315.
[18] L.W. McKeehan, Phys. Rev. 21 (1923) 402.
[19] A.J. Bradley, A.H. Jay, A. Taylor, Phil. Mag. 23 (1937) 5456.
[20] B.E. Warren, X-Ray Diffraction, Addison-Wesley, 1969, p. 253.
[21] C.V. Thompson, J. Appl. Phys. 58 (1985) 763.
[22] P. Wang, D.A. Thompson, W.W. Smeltzer, Nucl. Instrum. Methods B 7/8 (1986) 97.
[23] P. Wang, D.A. Thompson, W.W. Smeltzer, Nucl. Instrum. Methods B 16 (1986) 288.
[24] T. Veres, P. Desjardins, R.W. Cochrane, M. Cai, M. Rouabhi, L. Cheng, R. Abdouche, M. Sutton, Thin Solid Films, 382 (2001) 164.
[25] J.C. Liu, J.W. Mayer, Nucl. Instrum. Methods B 19/20 (1987) 538.
[26] J.C. Liu, J. Li, J.W. Mayer, J. Appl. Phys. 67 (1990) 2354.
[27] D.E. Alexander, G.S. Was, Phys. Rev. B 47 (1993) 2983.
[28] M. Born, E. Wolf, Principles of Optics, Pergamon, Oxford, 1964, p. 57.
[29] L.G. Parratt, Phys. Rev. 95 (1954) 359.
[30] Y. Huai, R.W. Cochrane, M. Sutton, Phys. Rev. B 48 (1993) 2568.
[31] H.H. Anderson, Appl. Phys. 18 (1979) 131.

[32] P. Sigmund, A. Gras-Marti, Nucl. Instrum. Methods 182/183 (1981) 25.
[33] F. Besenbacher, J. Bϕttiger, S.K. Nielsen, H.J. Whitlow, Appl. Phys. A 29 (1982) 141.
[34] H.H. Andersen, Appl. Phys. 18 (1979) 131.
[35] F. Pfeifer, C. Radeloff, J. Magn. Magn. Mater. 19 (1980) 190.
[36] D. Lederman, J.M. Gallego, S. Kim, I.K. Schuller, J. Magn. Magn. Mater. 183 (1997) 261.
[37] R.M. Bozorth, Phys. Rev. 70 (1946) 923.
[38] P.F. Carcia, A. Suna, J. Appl. Phys. 54 (1983) 2000.
[39] R.Q. Hood, L.M. Falicov, Phys. Rev. B 46 (1992) 8227.
[40] J. Barnas, A. Fuss, R.E. Camely, P. Grünberg, W. Zinn, Phys. Rev. B 42 (1990) 8110.
[41] T.G.S.M. Rijks, R. Coehoorn, W.M. de Jong, W.J.M. de Jonge, Phys. Rev. B 51 (1995) 283.